Journal of Catalysis 281 (2011) 241–253

Contents lists available at ScienceDirect

Journal of Catalysis

journal homepage: www.elsevier.com/locate/jcat

$SrO{\cdot}Al_2O_3$ mixed oxides: A promising class of catalysts for oxidative coupling of methane

Tinku Baidya [a], Niels van Vegten [a], René Verel [a], Yijiao Jiang [a], Maxim Yulikov [b], Thomas Kohn [b], Gunnar Jeschke [b], Alfons Baiker [a,*]

[a] Institute for Chemical and Bioengineering, Department of Chemistry and Applied Biosciences, ETH Zurich, Hönggerberg, HCI, CH-8093 Zurich, Switzerland
[b] Laboratory of Physical Chemistry, Department of Chemistry and Applied Biosciences, ETH Zurich, Hönggerberg, HCI, CH-8093 Zurich, Switzerland

ARTICLE INFO

Article history:
Received 27 January 2011
Revised 3 May 2011
Accepted 5 May 2011
Available online 15 June 2011

Keywords:
Oxidative coupling of methane
Strontium–aluminum oxides
Oxygen ion radicals
^{27}Al MAS NMR
EPR

ABSTRACT

Varying the composition of Sr–Al oxides, mixed as well as single phase compounds were prepared and characterized extensively by XRD, NMR, TEM, EPR, XPS, and TPD. Depending on synthesis method and precursors, Sr/Al-based materials with different crystalline phases (e.g., $Sr_3Al_4O_9{\cdot}2H_2O$, double perovskite, $SrAl_4O_7$, $SrAl_2O_4$, and $SrCO_3$) were obtained. Apart from these crystalline phases, several other species were present, as identified by solid state NMR and TG–MS. The ratio of tetrahedrally to octahedrally coordinated Al (Al^{IV}/Al^{VI}) in the Sr/Al mixed oxides increased from 0.5 (pure alumina) to 5.2 in Sr/Al = 1.25, as determined by solid state NMR. The performance of these catalysts in the oxidative coupling of methane depended on the Al^{IV}/Al^{VI} ratio, both activity as well as C_{2+} selectivity increased with increasing Sr-content. The catalyst with a Sr/Al ratio of 1.25 showed a performance comparable to the well-known catalyst 1.9%Mn–4%Na_2WO_4/SiO_2 under the conditions used (810 °C, CH_4:O_2 = 108:22, GHSV ~ 26,000 L/kg_{cat} h).

1. Introduction

Oxidative coupling of methane (OCM) with molecular oxygen to produce higher hydrocarbons, especially ethylene and ethane has been a topic of continuous interest during the past three decades. A wide variety of metal oxides; mainly alkali, alkaline earth, and rare earth oxides and to a minor extent transition metal oxide based catalysts have been studied [1–10]. In addition, many catalysts containing alkali metal or alkaline earth metal oxides as promoters have been investigated. Among the great variety of oxides explored for OCM, rare earth oxides, mainly M/La_2O_3 or Sm_2O_3 (M = Ca, Sr, Ba, etc.) belong to the most active, showing high ability to convert methane to higher hydrocarbon [12–18]. A yield of 18% or even slightly higher was reported over Sr and Ba doped La_2O_3 [14,15]. Fluorite oxides like M/ThO_2 show also comparable activity [19,20]. Other oxide systems like alkaline earth metal oxides, combination of their mixed phases and alkali metal modified analogs have also been studied [21–27]. Alkaline earth metal oxides are more active with additives like Al_2O_3, SiO_2 or other oxides of the same series due to lowering of carbonate decomposition temperature [28–31]. However, these oxides are normally less active than La_2O_3 based oxides, but show comparable selectivity. Among the various transition metal based oxides modified by alkali metal oxides reported in the literature, $Mn/Na_2WO_4/SiO_2$ stands out as a potential OCM catalyst [32–35].

Methane coupling reaction initiated by two possible active oxygen species were identified, namely: (i) molecular species such as O_2^- and O_2^{2-} for lanthanide oxides [36,37], and (ii) dissociated oxygen species such as nucleophile ions $O^{\cdot-}$ of the catalyst lattice [22,38,39]. Different oxide systems have different structural feasibility of oxygen radical generation at the oxide ion vacancy depending on p-type conductivity. The rare earth oxide based catalysts are interesting due to their intrinsic ability to form active O_2^- species and they are highly movable in the hexagonal structure [40–44]. On the other hand, due to low ionic conductivity in the compact perovskite structures, their activity is fairly low [45]. The origin of activity in alkaline earth metal oxides is related to the basic properties increasing from BeO to BaO. More basic oxides like SrO and BaO are more active at high temperature due to decomposition of surface carbonates providing crystal defect and therefore, low coordination surface oxides [46]. Activity was further enhanced by addition of alkali metal ions that promote formation of $Li^+O^{\cdot-}$ and $Na^+O^{\cdot-}$ type of pair near the oxygen vacancy site in MgO and CaO [25]. Several transition metal oxides modified with alkali metals also show improved selectivity due to peroxide like intermediate formation. Tetrahedral WO_4 surface species with one W═O and three W—O—Si surface bonds where proposed as the OCM active

* Corresponding author. Fax: +41 44 632 11 63.
E-mail address: baiker@chem.ethz.ch (A. Baiker).

0021-9517/$ - see front matter © 2011 Elsevier Inc. All rights reserved.
doi:10.1016/j.jcat.2011.05.005

sites in $Mn/Na_2WO_4/SiO_2$ [32]. Later a clear correlation between performance of this catalyst formulation and the support structure in the final calcined material was evidenced [34].

$SrCO_3$ decomposes at high temperature under OCM conditions, where CO_2 is present. Addition of additives like Al_2O_3 could lower the decomposition temperature promoting formation of SrO [30]. Such type of modification has been reported earlier [30]. In a recent study [47], $12SrO{\cdot}7Al_2O_3$ was found to promote the generation of oxygen radicals, a characteristic which could be useful in OCM. However, this oxide is metastable and decomposes into more stable Sr–Al compounds, $Sr_3Al_2O_6$ and $SrAl_2O_4$, at elevated temperatures [47,48]. Also, the catalytic properties of the oxide were found to depend strongly on synthesis parameters, such as heating rate, water content of the environment, and especially the Sr/Al ratio in the precursor material [47]. Due to the fact that different Sr–Al compounds have different kinetics of formation and temperatures of decomposition [49], the properties of the product depend on many synthesis parameters. Some examples of stable Sr–Al phases which were obtained are hexaaluminate [50], spinel [51], perovskite [52], and $SrAl_4O_7$ [53].

The aim of the present study was to investigate the effect of synthesis method, Sr/Al ratio, and precursor materials on the structural properties of Sr–Al oxides and to explore the catalytic potential of these materials for the oxidative coupling of methane. The materials were structurally characterized by a number of complementary techniques, such as XRD, solid state NMR, electron microscopy, EPR, XPS, and thermogravimetry.

2. Experimental

2.1. Catalyst preparation

Sr–Al mixed oxides were prepared by co-precipitation of the metal hydroxides. $Al(NO_3)_3$ and $Sr(NO_3)_2$ were dissolved in water and the hydroxides were precipitated by addition of an excess amount of ammonia solution (pH = 11), stirred vigorously and heated to dryness. The dried material was calcined at 800 °C for 12 h and subsequently crushed and sieved to 60–100 micron grain size. The mixed oxide samples are denoted as Sr/Al-*x* (where *x* represents the Sr/Al atomic ratio and varies between 0.25 and 1.5).

Single phase Sr–Al oxides were prepared by different methods. $SrAl_2O_4$ was prepared by solution combustion of stoichiometric amounts of $Al(NO_3)_3$ and $Sr(NO_3)_2$ using urea as fuel in a 300 ml Pyrex glass dish [54]. The solution was placed in a pre-heated furnace at 600 °C and after evaporation the combustion started. The oxide product was obtained within one minute and kept at 800 °C for 12 h to remove carbonaceous residues. $Sr_3Al_2O_6$ was prepared by the citric acid gel method [52], in which stoichiometric amounts of $Al(NO_3)_3$ and $Sr(NO_3)_2$ were dissolved in water with excess amounts of citric acid and ethylene glycol. With continuous heating at ~100 °C under constant stirring to evaporate superfluous water, the volume of the solution decreased and the solution viscosity increased continuously due to gradual polymerization. The viscous mass was further heated at ~150 °C which accelerated esterification of citric acid and ethylene glycol and eliminated the remaining water, producing an amorphous resin. This resin was calcined in air at 800 °C for 12 h. $SrAl_4O_7$ was prepared by taking stoichiometric amounts of nitrate precursors and applying the same procedure as in the citric acid gel method [53]. The dried gel was calcined in air at 950 °C for 12 h.

Other samples were prepared by impregnation of Al_2O_3 with Sr-acetate, nitrate or hydroxide. These Sr precursors were dissolved in water followed by addition of γ-Al_2O_3 (Degussa, SSA = 180 m^2/g) and after evaporation the material was calcined at 800 °C in a furnace for 12 h. These samples are denoted as Sr/Al-1.25A, Sr/Al-1.25N, and Sr/Al-1.25H for the acetate, nitrate, and hydroxide precursors, respectively.

As a reference catalyst, $1.9\%Mn–4\%Na_2WO_4/SiO_2$ was synthesized according to the procedure reported by Jiang et al. [55]. In brief, the catalyst was prepared by mixing a slurry of $Mn(NO_3)_2$, Na_2WO_4, and silica gel (amorphous, 60–100 μm mesh). After drying, the catalyst was calcined at 800 °C for 8 h.

2.2. Catalyst characterization

Nitrogen physisorption isotherms (adsorption–desorption branches) were measured on a Micromeritics ASAP 2000 instrument at 77 K. Samples were outgassed for 1 h under vacuum at 400 °C before measurement and the specific surface area (SSA) was determined using the BET method. X-ray diffractograms were recorded on a Siemens D5000 using Cu $K\alpha_1$ (λ = 1.54056 Å) radiation in step mode between 20 and 80° 2θ with a step-size of 0.02° and 8 s/step. For transmission electron microscopy (TEM), the material was dispersed in ethanol and few drops were deposited onto a perforated carbon foil supported on a copper grid. TEM investigations were performed on a CM30ST microscope (FEI; LaB_6 cathode, operated at 300 kV, point resolution ~2 Å).

^{27}Al MAS NMR measurements were performed on a Bruker Avance 700 spectrometer (Bruker, Karlsruhe, Germany) at a resonance frequency of 182.4 MHz for ^{27}Al nuclei. All ^{27}Al shifts are referenced to a 0.1 M aqueous solution of $Al(NO_3)_3$. For the 1D experiments in Figs. 5 and 6, the NMR spectra were recorded using a 4 mm Bruker double resonance probe at a spinning frequency of 15.00 kHz. A single-pulse excitation with a flip angle of $\pi/6$ and a repetition time of 0.5 s was used and a total of 200 scans were accumulated for the mixed oxides, while 800 scans were used for the spectra of the $SrAl_4O_7$, $SrAl_2O_4$, $Sr_3Al_2O_6$ single phase compounds. The data were processed using the XWINNMR software (Bruker, Karlsruhe, Germany). The quantification of the Al^{IV}/Al^{VI} ratio in Fig. 6 was calculated by numerical integration of the spectral regions between ca. 100 and 40 ppm for Al(IV) and Al(VI) between 25 and −25 ppm. For the 1D and 2D experiments presented in Fig. 7, a 2.5-mm Bruker double resonance probe was used at a spinning frequency of 20.00 kHz. The 1D spectra were acquired using a single-pulse excitation with a flip angle of approximately $\pi/6$, a recycle delay of 1.0 s and 1024 scans. The 2D MQMAS experiments were implemented using a shifted echo method with a selective π pulse of 40 μs duration before acquisition of the full echo [56,57]. The phase cycle selected the 3Q coherence during t_1. The hard pulses for excitation and conversion were experimentally optimized and found to be 3.25 and 0.90 μs. A total of 256 increments with a dwell time of 10 μs in t_1 were acquired with 1056 scans per increment for the experiments in Fig. 7a and c and 720 scans for the experiment in panel b. All used a recycle delay of 0.5 s. The 2D spectra were processed by zero filling once to 1024 points, performing a circular shift of the data points in t_2 such that the echo maximum coincided with the start of the FID and apodisation with a 256 Hz Gauss function adapted to the full echo nature of the signal. After the Fourier transform in the direct dimension, the data was zero filled once to 256 points in t_1. A complex Fourier transform without apodisation in the indirect dimension produced the 2D spectra. The scale in the indirect dimension follows the convention by Amoureux and Fernandez [58,59]. The spectrum in Fig. 7b was subsequently scaled by a factor of 22/15 to compensate for the smaller number of scans and to bring all spectra to the same absolute intensity scale. The contour levels in Fig. 7a–c are located at the same absolute values with the lowest level set to ten times the standard deviation of the noise in panels a and c, and to 8.25 times the standard deviation of the noise for the spectrum in Fig. 7 b. The contour levels are spaced by a factor of 1.3. The

MatNMR toolbox within the Matlab environment (www.mathworks.com), was used to process the data [60].

X-ray photoelectron spectra of the Sr–Al-*x* oxides were recorded on a Thermo Fisher Scientific Multilab 2000 (England) instrument with Al Kα radiation (1486.6 eV). The binding energies reported here are with reference to graphite at 284.5 eV or Ag($3d_{5/2}$) at 368.2 eV having an accuracy of (0.1 eV). Oxide samples were made into thin pellets at room temperature, and XPS data were recorded.

Thermogravimetric (TG) experiments were performed on a Netzsch STA 449 C thermoanalyzer. The exhaust gas was analyzed by an Omnistar (Pfeiffer Vacuum) mass spectrometer connected to the thermoanalyzer by a heated stainless steel capillary. Temperature Programmed Desorption (TPD) was performed with a flow of 50 mL/min He and a heating rate of 10 K/min to 1150 °C.

Continuous-wave (CW) EPR spectra were acquired on a Bruker Elexsys E500 X-band spectrometer (microwave frequency 9.48 GHz) at 130 K. The maximum incident microwave power for this spectrometer was 200 mW (at 0 dB attenuation). The spectrometer was equipped with a super-high Q resonator (ER 4122 SHQ) and a He-flow cryostat (ESR 910, Oxford Instruments). Spectral simulations of CW EPR powder patterns were done using the Matlab package EasySpin [61].

2.3. Catalytic tests

The reactor set-up was a conventional gas flow system where methane (99.5% PanGas) and oxygen (99.999%, PanGas) were co-fed over the catalyst. The catalyst was placed in a quartz U-tube reactor (ID 4.5 mm) which itself was placed inside a temperature controlled furnace. Typically, 300 mg of catalyst (60–100 μm mesh) was diluted with 200 mg of quartz sand and kept in place between two quartz wool plugs. Gas flows were regulated by mass flow controllers (Brooks Instruments B.V., model 5850E), and were fixed at 108 mL/min CH_4 and 22 mL/min O_2, yielding a total flow of 130 mL/min and a CH_4/O_2 ratio of 5. This resulted in a gas hourly space velocity of 26,000 L/kg_{cat} h. Due to the fact that the $SrAl_2O_4$, $SrAl_4O_7$ as well as the Al_2O_3-derived oxides did not form stable pellets after pressing, these materials were tested with a reduced catalyst mass (125 mg instead of 300 mg) to prevent blocking of the reactor. For the sake of comparison, the $Sr_3Al_2O_6$ single phase oxide was tested at both 125 and 300 mg, keeping the gas flows the same. This resulted roughly in a twice as high rate of reaction (see both entries for $Sr_3Al_2O_6$ in Table 2).

The temperature was measured by a thermocouple well on the outer surface of the quartz reactor at the middle of the catalyst bed. Reactions were performed at a fixed temperature of 810 °C. The exhaust gas was analyzed using an on-line gas chromatograph (6890N, Agilent Technologies, CarbonPLOT column and fitted with TCD and FID) connected to the reactor with heated stainless steel lines. The GC was able to fully separate exhaust gas components such as O_2, CO, CO_2, CH_4, C_2H_2, C_2H_4, C_2H_6, C_3H_6, and C_3H_8. Each of the products was calibrated against a calibration gas mixture. A blank run (quartz tube filled with only quartz wool and quartz sand) showed no conversion at the reaction conditions used. Initial experiments in which catalyst mass and temperature were varied were used to optimize experimental settings for Sr/Al-1.25 (based on complete conversion of oxygen). The freshly prepared Sr-rich oxide, exposed to air at room temperature for at least 3 h, is designated as stored catalyst.

Methane conversion was defined as: X_{CH_4} (%) = (moles of CH_4 equivalent of carbon products × 100)/moles of CH_4 in feed. Selectivity toward C_n products (ethylene + ethane + propane + propylene) was defined as: S (%) = Σ((n × moles of C_n products) × 100)/(moles of CH_4 equivalent of carbon products), where n corresponds to the number of carbon atoms, generally 2 and 3 here. The carbon balance varied depending on the catalyst material but was always better than 90%.

3. Results

3.1. Textural and structural properties

The catalysts were characterized with regard to their textural and structural properties. The specific surface areas (SSAs) of the Sr–Al oxides are listed in Table 1. The surface areas consistently decreased with increasing Sr/Al ratio (Sr/Al-0.25 to 1.25) from 73 to 0.5 m^2/g. Single phase Sr–Al oxides ($SrAl_4O_7$, $Sr_3Al_2O_6$, and $SrAl_2O_4$) had surface areas ranging from 1.5 to 10 m^2/g. The Sr–Al samples (Sr/Al ratio 1.25) derived from alumina and strontium hydroxide, nitrate, and acetate precursors afforded specific surface areas of 0.4, 1.3, and 4.5 m^2/g, respectively. The reference catalyst 1.9%Mn–4%Na_2WO_4/SiO_2 had a surface area of 0.5 m^2/g, comparable to the value reported for the catalyst used in [33], but lower compared to that of Ref. [55].

Fig. 1 presents the XRD patterns of Sr–Al mixed oxides with a Sr/Al ratio from 0.25 to 1.5 and shows the presence of several crystalline phases in the mixed oxides. Phases identified in the different samples are listed in Table 1. XRD patterns of single phase compounds such as $SrAl_4O_7$, $SrAl_2O_4$, $Sr_3Al_2O_6$, and $SrCO_3$ are displayed in Fig. 2a. The reflections related to the single phase Sr–Al oxides fit to their respective JCPDS patterns (1-070-1479, 10-0061, and 24-1187 for $SrAl_4O_7$, $SrAl_2O_4$, $Sr_3Al_2O_6$, respectively). Analysis of the mixed phase oxide patterns indicated the presence of multiple crystalline phases. Predominately reflections of $Sr_3Al_2O_6$ were found, which relative intensity increased with increasing Sr/Al ratio. Its reflections were narrow, indicating a relatively large crystallite size. Other reflections, observed at low Sr loading (marked by asterisk in Fig. 1) gradually vanished with increasing Sr/Al ratio until the Sr/Al ratio reached 1.5. These reflections were sharp and fitted well to $Sr_3Al_4O_9{\cdot}2H_2O$ (JCPDS 32-1221), a hydrated Sr–Al phase. However, their relative intensity was low compared to $Sr_3Al_2O_6$.

Fig. 2b shows the XRD patterns of the Sr–Al oxides prepared by reaction of different Sr–salts with Al_2O_3. As emerges from Fig. 2b, the formation of the crystalline phase highly depended on the type of precursor. With the acetate precursor, a mixture of $SrCO_3$ and $Sr_3Al_2O_6$ was formed, whereas nitrate salt produced $Sr_3Al_2O_6$ as only detectable phase. The hydroxide precursor tended to form a mixture of $Sr_3Al_2O_6$ and $Sr_{12}Al_{14}O_{33}$ (JCPDS 40-0025) phases (latter

Table 1
BET specific surface area (SSA) and mass loss upon heating in He up to 1150 °C. Numbers in brackets indicate the values obtained for the fresh materials (i.e., characterized within 3 h after synthesis). The crystalline phases as observed by XRD are; 0 = Al_2O_3, A = $Sr_3Al_4O_9{\cdot}2H_2O$, B = double perovskite, C = $SrAl_4O_7$, D = $SrAl_2O_4$, E = hydroxide $Sr_{12}Al_{xx}O$ and F = $SrCO_3$.

Catalyst	BET SSA (m^2/g)	Mass loss (wt.%)	Phases
Al_2O_3	123	8.6	0
Sr/Al-0.25	73	8.1	A
Sr/Al-0.33	62	5.4	A + B
Sr/Al-0.50	25	5.4	A + B
Sr/Al-0.75	8	6.0	A + B
Sr/Al-0.86	3	–	A + B
Sr/Al-1.0	1.2	8.9 (4.6)	A + B
Sr/Al-1.25	0.5	4.5 (2.9)	B
Sr/Al-1.5	0.5	2.7	B
$SrAl_4O_7$	10	–	C
$SrAl_2O_4$	1.4	1.0	D
$Sr_3Al_2O_6$	7	–	B
Sr/Al-1.25H*	0.4	–	B + E
Sr/Al-1.25 N*	1.3	–	B
Sr/Al-1.25A*	4.5	–	B + F

* Samples where Sr salt was impregnated on Al_2O_3.

Table 2
Catalytic results. Standard reaction conditions were: 300 mg catalyst with 200 mg SiO_2 diluent (both 60–100 μm mesh size) a total flow of 130 mL/min (CH_4 = 108 mL/min, O_2 = 22 mL/min), temperature = 810 °C. For the entries marked by the asterisk (*), 125 mg catalyst was used instead of the standard 300 mg, for reasons specified in the text (Section 2). This 125 mg catalyst was mixed with 375 mg SiO_2 to obtain a similar bed volume. Otherwise all parameters were similar.

Catalyst	X_{CH_4} (%)	S_{Total} (%)	C_2H_4/C_2H_6	C_{2+} yield	Rate (mol m^{-2} h^{-1})
Al_2O_3	14	16	1.3	2	0.001
Sr/Al-0.25	20	37	1.7	7	0.002
Sr/Al-0.33	21	46	1.9	10	0.003
Sr/Al-0.50	23	57	2.0	13	0.008
Sr/Al-0.75	26	61	1.9	16	0.029
Sr/Al-0.86	26	61	1.8	16	0.078
Sr/Al-1.0	27	63	1.7	17	0.202
Sr/Al-1.25	28	63	1.7	18	0.503
Sr/Al-1.5	6	64	0.6	4	0.108
$SrCO_3$	6	61	0.7	4	–
$SrAl_4O_7$*	9	54	1.2	5	0.019
$SrAl_2O_4$*	27	59	2.1	16	0.416
$Sr_3Al_2O_6$	27	54	2.9	15	0.035
$Sr_3Al_2O_6$*	22	51	–	11	0.068
Sr/Al-1.25H*	10	54	0.9	5	0.539
Sr/Al-1.25N*	18	58	1.5	10	0.298
Sr/Al-1.25A*	29	62	1.7	18	0.139
$Mn–Na_2WO_4/SiO_2$	18	68	1.9	12	0.323
$5\%Sr/La_2O_3$[a]	25	63	0.4	16	0.3

[a] Data taken from Ref. [20].

marked by +) in Fig. 2b. The latter phase is the same as reported in [47,48].

Fig. 3 shows selected TEM images (a, b) and electron diffraction (ED) patterns (a′, b′) of $Sr_3Al_2O_6$ (a) and Sr/Al-1.0 (b). Single phase $Sr_3Al_2O_6$ showed clear lattice fringes and at three different positions similar ED patterns were observed. A constant Sr/Al ratio was found by EDX mapping at four different positions of a few microns in diameter (see Fig. 4a). On the other hand, the mixed phase Sr–Al oxides did not possess clear fringes and EDX mapping showed a non-constant Sr/Al ratio at four different positions in the sample (see Fig. 4b). Additionally, ED showed only reflections at certain positions, and this electron diffraction pattern was consistent with that of the pure $Sr_3Al_2O_6$ sample. These observations indicate a non-homogeneous distribution of the crystalline phase ($Sr_3Al_2O_6$) in the mixed phase oxides and the presence of poorly crystalline material. Similar results were obtained for Sr/Al-0.5, indicating a certain universality of this behavior.

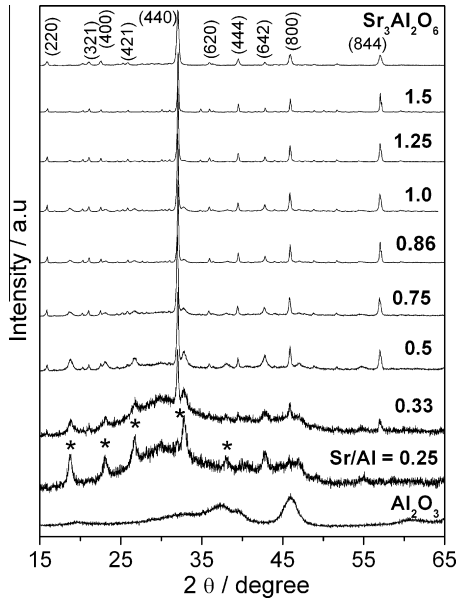

Fig. 1. XRD pattern of the mixed phase oxides with Sr/Al ratio varying from 0.0 to 1.5.

^{27}Al MAS NMR uncovered the presence of differently coordinated Al in the Sr/Al-*x* oxides, as shown in Fig. 5. In these mixed phase oxides, signals at ~65 and 10 ppm were observed indicating the presence of both tetrahedrally (65 ppm) as well as octahedrally (10 ppm) coordinated Al species [62,63]. Pure Al_2O_3 (Sr/Al-0) showed two broad peaks at ~65 and 10 ppm, respectively. Upon increasing the Sr-content of the material, the intensity of the broad peak at ~10 ppm was reduced and a sharp peak was superimposed at a Sr/Al ratio of 0.75 and above. This broad feature slowly vanished at higher Sr-contents. The peak visible at ca. 65 ppm showed a more complex behavior, and upon increasing the Sr-content its relative intensity increased and sharper features were observed.

In order to assign the differently coordinated Al species in the mixed phase systems, single phase oxide spectra were analyzed as well. Fig. 6 shows the ^{27}Al MAS NMR spectra of the single phase Sr–Al oxides ($SrAl_2O_4$, $Sr_3Al_2O_6$, and $SrAl_4O_7$). $SrAl_2O_4$ and $Sr_3Al_2O_6$ showed rather sharp peaks at ~65 and ~10 ppm, respectively. $SrAl_4O_7$ contained some octahedrally coordinated Al, and based on the peak around 65 ppm, several Al^{IV} species with a rather well-ordered local environment were present. In general, the peaks obtained for the single phase oxides were sharper compared to those obtained for the mixed phase oxides.

Due to their high specific activity (*vide infra*), Sr/Al-1.25 and Sr/Al-1.25H were analyzed in-depth by 2D MQMAS, the results of which are presented in Fig. 7. The 2D spectra show the spectral region characteristic for tetrahedrally coordinated Al species [62,63]. The spectrum of as-prepared Sr/Al-1.25 (Fig. 7a) showed a number of species to be present. Two narrow "ridges" belonging to two well-ordered Al^{IV} species with a significant quadrupolar coupling constant, as testified by the width of these two lines in the direct dimension were observed, along with a much less ordered Al^{IV} species around 70 ppm. A weak shoulder superimposed on this peak toward higher ppm values is also visible. The 1D spectrum (panel d, bottom) shows that very little octrahedral Al is present in this sample. The same material calcined at 1000 °C (Fig. 7b) basically shows the same features except that the shoulder is now clearly resolved into a separate signal with a maximum at 76 ppm. In addition, the relative intensity of the less ordered peak has decreased significantly compared to the two signals corresponding to the two highly ordered sites. The width of this signal also seems to be decreased compared to the one in panel a, possibly indicating a higher amount of order. No Al^{VI} could be detected in this sample.

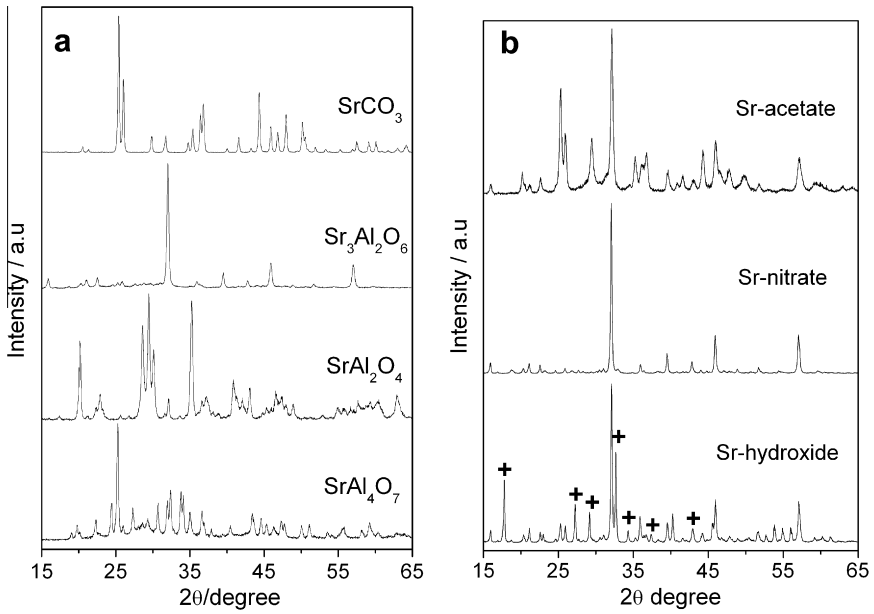

Fig. 2. (a) XRD pattern of the single phase oxides ($SrAl_4O_7$, $SrAl_2O_4$, and $Sr_3Al_2O_6$). (b) XRD pattern of the Sr impregnated Al_2O_3 samples with various Sr precursors.

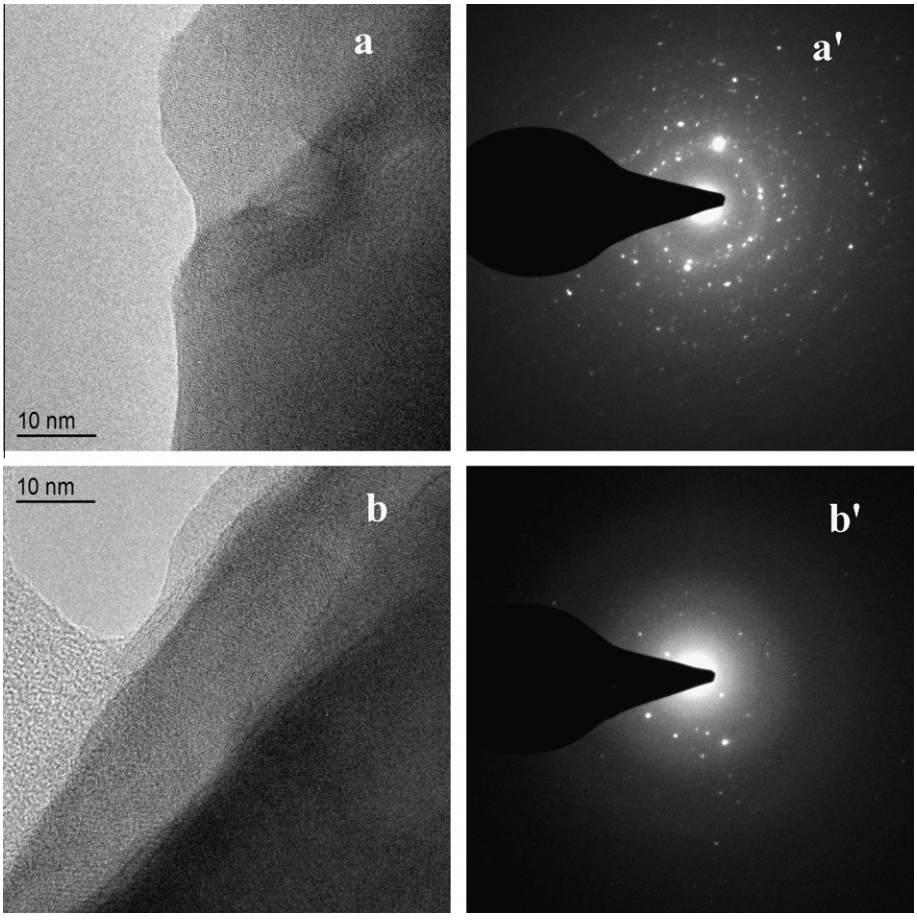

Fig. 3. TEM and ED of single phase $Sr_3Al_2O_6$ and mixed phase Sr/Al-1.0.

The Sr/Al-1.25H had a significant signal around 10 ppm, demonstrating the presence of Al^{VI}. Several Al^{IV} species were present, with features resembling those of the as-prepared Sr/Al-1.25. Clear similarities were observed in two ridge like features extending between 40 and 70 ppm in the direct dimension. These, we tentatively assign to the Al^{IV} species in the $Sr_3Al_2O_6$ double perovskite, the presence of the two signals in the 2D spectra being consistent with the two inequivalent Al sites in the crystal structure. In addition, a third line with a significant quadrupole coupling constant is observed parallel to the two signals originating from the

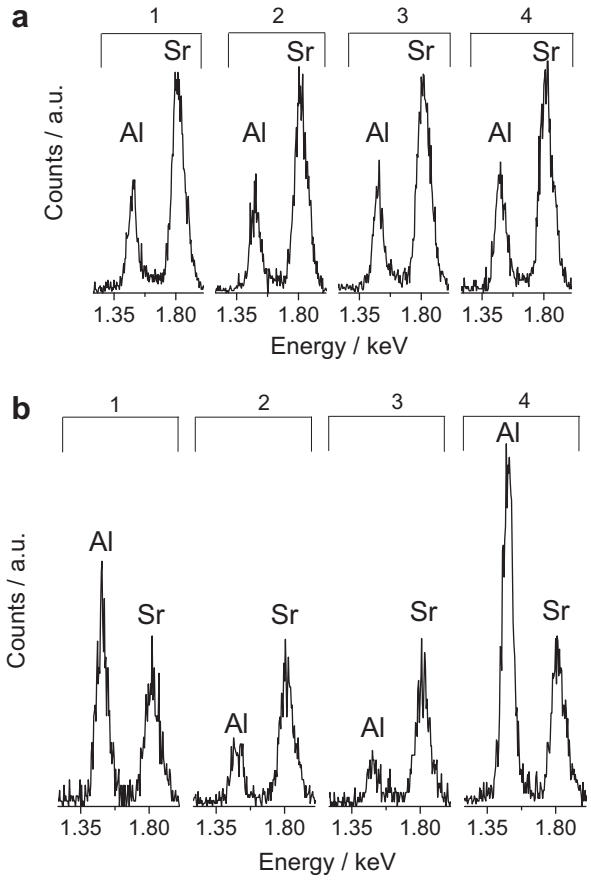

Fig. 4. EDX analysis of: (a) single phase $Sr_3Al_2O_6$ and (b) mixed phase Sr/Al-1.0.

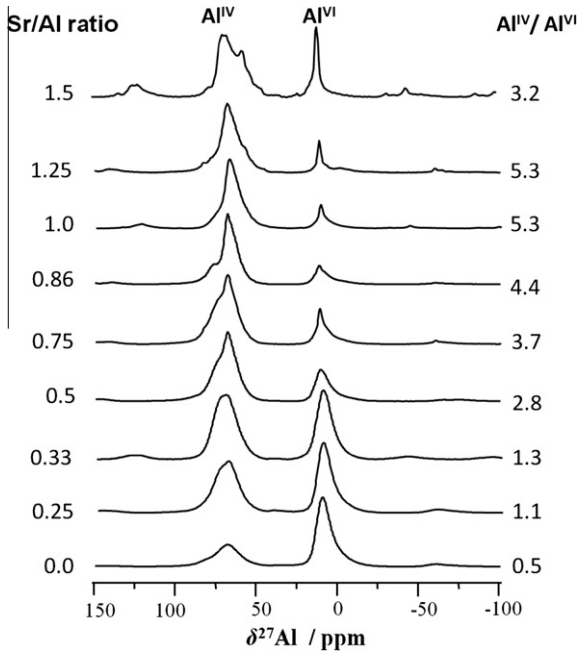

Fig. 5. ^{27}Al NMR spectra of Sr–Al mixed oxides with varying Sr/Al ratio from 0.0 to 1.5. The Al^{IV}/Al^{VI} ratio is shown on the right-hand side.

double perovskite. This third line however is broader in the indirect dimension indicating less order, or possibly an overlap of several sites. The final feature has a shift of 70 ppm (equal to the feature around 70 ppm of the as-prepared Sr/Al-1.25 sample in panel a). It is however shifted in the indirect dimension and has a smaller line width and a more symmetric shape. Both factors taken together indicate a smaller distribution of the quadrupolar coupling constant. The 1D spectrum of Sr/Al-1.25H displays a strong peak for Al^{VI} around 10 ppm.

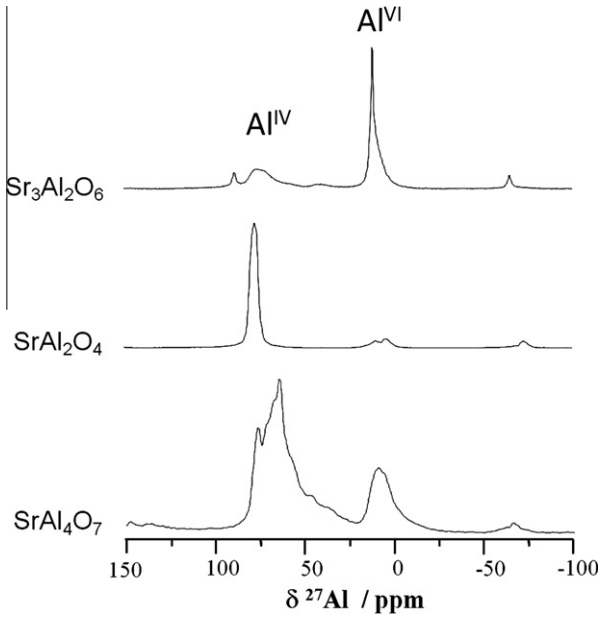

Fig. 6. ^{27}Al NMR spectra of the $SrAl_4O_7$, $SrAl_2O_4$, and $Sr_3Al_2O_6$ single phase reference compounds.

Fig. 8 shows the O(1s) XPS core level spectra of Sr–Al mixed oxides with different Sr/Al ratio. Clearly, the signal becomes non-symmetrical toward higher binding energy with increasing Sr/Al ratio. Deconvolution of the spectra shows the presence of two peaks at ~529.7 eV and ~531.5 eV, attributed to O^{2-} and carbonate oxygen species, respectively. The higher binding energy peak position and FWHM match with pure carbonate signal. Similar spectra were also reported for MgO and $BaCO_3$ systems [64]. The relative intensity of carbonate oxygen species increases with the Sr/Al ratio. The concentration of Sr on the surface indicated slight segregation.

Temperature programmed desorption (TPD) was performed on the Sr–Al mixed phase materials and on selected single phase oxides. The weight loss due to decomposition/desorption up to 1150 °C is listed in Table 1. By mass spectrometry (MS), the evolution of four species was observed: H_2O, NO, O_2, and CO_2 (m/z = 18, 30, 32, and 44, respectively). Fig. 9a shows the MS-traces of H_2O, NO, and CO_2 recorded during TPD of Sr/Al-0.33, 1, and 1.25.

Water evolved from the sample in two distinctly different manners: for low Sr/Al ratios (0.25–0.5), a rather broad desorption profile was observed between 50 and 450 °C. This was attributed to desorption of physisorbed water and recombination of terminating surface hydroxyl groups. At higher Sr/Al ratios, occasional sharp increases in the m/z = 18 signal were observed between 50 and 530 °C, along with sharp decreases in the TG signal (see Fig. 9b). Similar behavior was observed for the evolution of CO_2: at lower Sr/Al ratios a broad profile was observed. For Sr/Al ratios of 0.75 and above, the broad profile dominating at lower temperature was lacking almost entirely, and sharper high temperature features evolved instead. These consisted of a main signal with the maximal rate of desorption centered at 810 °C and a smaller centered at 960 °C. Simultaneous with the feature around 960 °C, a sharp increase in the m/z = 30 and 32 signals was observed as well. The m/z = 30 signal, indicative of NO, is plotted in Fig. 9a for three representative samples.

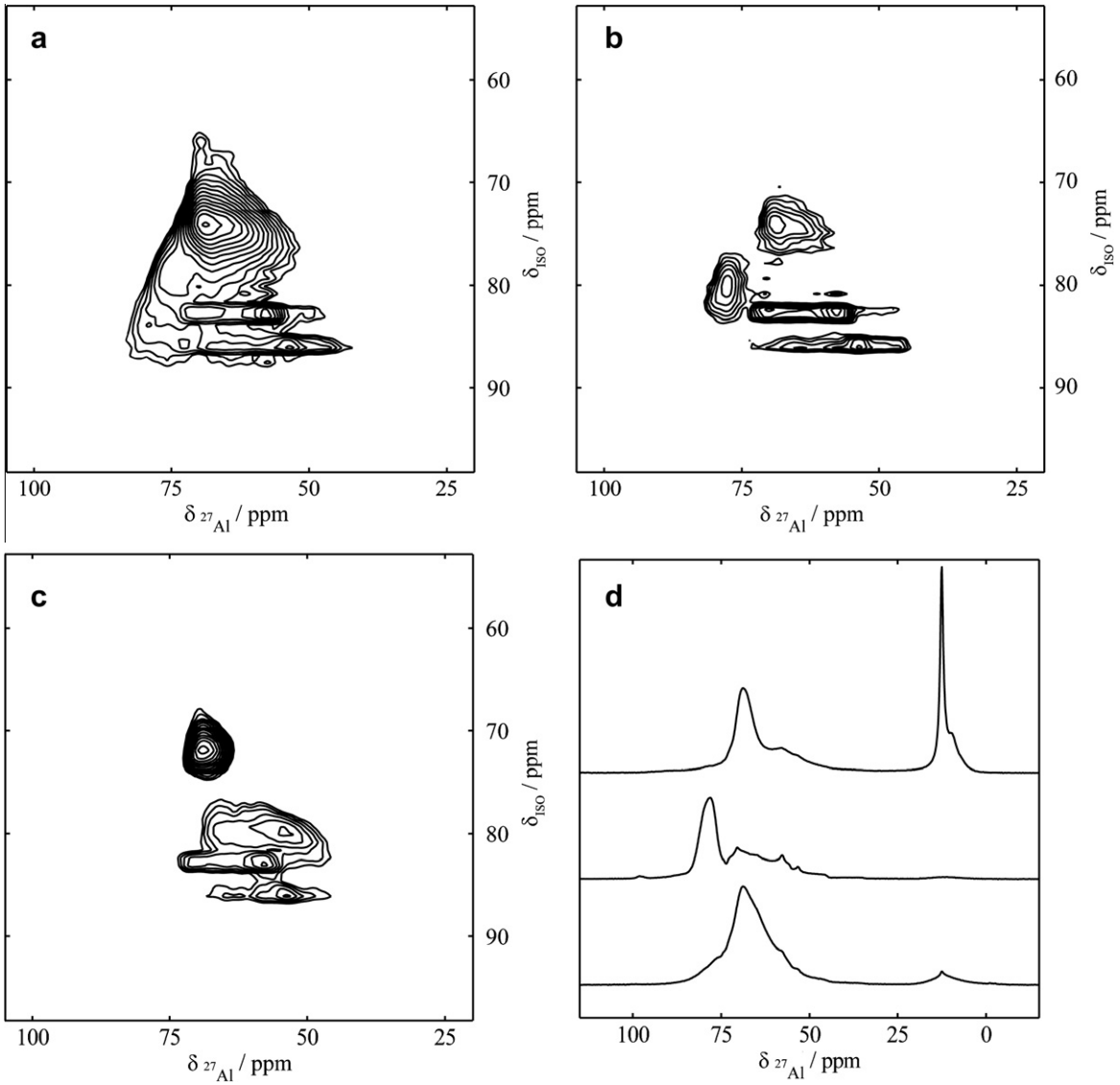

Fig. 7. ^{27}Al 2D MQMAS NMR spectra (a–c) and corresponding ^{27}Al 1D MAS NMR spectra (d) of three Sr–Al–O compounds. Sr–Al mixed oxide with Sr/Al = 1.25 (a) and (d, bottom). Sr/Al mixed oxide with Sr/Al = 1.25 after calcination at 1000 °C (b) and (d, middle). Sr–Al mixed oxide with Sr/Al = 1.25 prepared from Sr-hydroxide precursor (c) and (d, top).

Fig. 9b shows the TG traces of TPD experiments on fresh and stored (see Section 2) Sr/Al-1 and 1.25. The stored material displayed more features, especially in the lower temperature range (below 800 °C). These differences were highlighted by representing the data in its differential form (DTG, Fig. 9c). The negative peaks in Fig. 9c corresponded to a concurrent increase of the MS signals of H_2O (minima at 75, 250, and ca. 400 °C), CO_2 (minimum at ca. 830 °C) and CO_2 with NO and O_2 (minimum at ca. 1000 °C).

EPR measurements revealed a qualitative difference between the single phase and the mixed phase oxides. In the $Sr_3Al_2O_6$ pure phase sample, no EPR signals were detected in the as-prepared and O_2 treated sample. In the EPR spectrum of the Sr/Al-1.25 mixed phase oxide system, we observed three types of signals. In the low field region, several EPR lines were detected with most intense absorption at around $g = 4.2$ (spectra not shown). The shape and the intensity of this part of the spectrum did not change upon any treatment of the sample, thus we consider this signal not to be related to the chemical activity of the oxide. We attribute this signal to paramagnetic impurities in the Sr–Al mixed phase oxide.

In the field range at around $g = 2.0$, two other EPR signals were observed (Fig. 10). The first signal has relatively short relaxation times. At 130 K, this signal is not saturated up to an incident microwave power of 3.2 mW (18 dB attenuation). The corresponding EPR spectrum can be simulated as an isolated electron spin ½ with nearly axial g-tensor ($g_x = 2.0012$, $g_y = 2.0072$, $g_z = 2.0856$) (Fig. 10a). These g-values are close to those reported for the O_2^- species formed in the $12CaO{\cdot}7Al_2O_3$ system, $g = [2.002, 2.008, 2.074]$ [65].

The second paramagnetic species observed at this field range had significantly different relaxation properties. At 130 K, the intensity of the corresponding EPR signal was in the linear regime with respect to the square root of the incident microwave power only below 12 μW (attenuation of 42 dB). This type of EPR spectrum could be simulated with an assumption of one electron spin ½ coupled to a nuclear spin of 1 (Fig. 10b). The only nucleus with nuclear spin 1 that can be present in the studied system was ^{14}N, originating from incomplete conversion of the parent nitrate (see TPD results above, and discussion furtheron in the text). Therefore, we assigned the spectrum to a nitrogen containing species appearing from thermal decomposition of remaining nitrate precursor.

The EPR spectra appearing from nitrogen containing inorganic radical species were reported for different oxide supports [44].

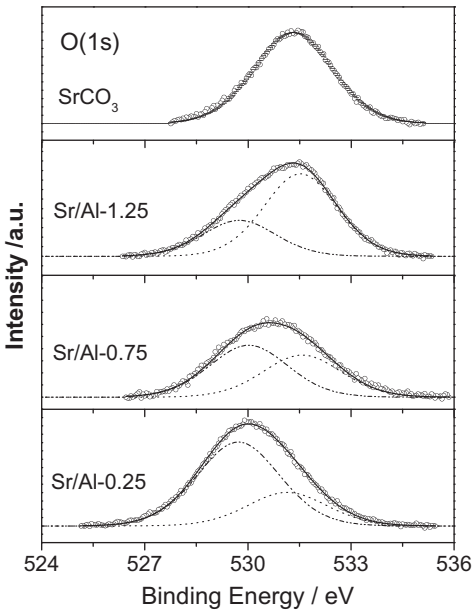

Fig. 8. O(1s) XPS core level spectra of Sr/Al-*x* (0.25, 0.75, and 1.25) and $SrCO_3$.

The main types of paramagnetic species discussed so far are NO [66–71], NO_2 [68], NO_2^{2-} [67,71] and $N_2O_2^-$ [72].

An EPR spectrum very similar to the spectrum of the second type of species reported here was observed for NO molecules adsorbed on magnesium oxide [67]. In the cited reference, the mentioned EPR spectrum was assigned to an NO_2^{2-} species formed on the surface of MgO from NO molecules and surface O^{2-} ions. For NO adsorbed at lower temperatures, a different EPR spectrum has been observed and attributed to an NO molecule in a strong crystalline field where the splitting of the doublet π-antibonding level is large and the unpaired electron is mainly confined to one level. In such a situation, a stronger *g*-anisotropy was observed in agreement with the expectations for a system with a low lying excited state. In the NO_2^{2-} species, the degeneracy of the ground electronic state is removed which leads to weaker *g*-anisotropy [67].

We can exclude formation of paramagnetic species containing two nitrogen atoms like $N_2O_2^-$ in our system because no hyperfine splitting due to the second nitrogen is experimentally observed. Thus, the assignment of the species under discussion is restricted to either neutral or doubly charged NO_2.

Following the argumentation of Lunsford [67], we rather attribute the discussed EPR spectrum to NO_2^{2-}, resulting from the decomposition products of residual entrapped nitrate precursor. As we simultaneously observe the formation of O_2^-, it is feasible to assume that these are NO_2^{2-} species formed after homolysis of NO_3^- from an NO molecule and an O^{2-} ion from the oxide phase with one free coordination position. Such a formation should be possible on the surface of the amorphous phase. Exposure to methane (*vide infra*) strongly reduced the intensity of both O_2^- and NO_2^{2-} EPR signals (see Fig. 11 spectra d), providing further evidence of the presence of these species on the surface.

The homogeneous line width of the observed EPR spectrum attributed to NO_2^{2-} can be estimated to be less than 0.15 mT. For such a narrow line any dipolar field from neighboring paramagnetic centers down to 0.1–0.2 mT should be visible in the spectrum. One can therefore estimate that the surface concentration of paramagnetic centers is rather low such that the mean distance to the next neighbor is not less then approximately 1.5–2 nm (as calculated from the magnetic dipolar field of an unpaired electron with $g \approx 2.0$ [73]) for the majority of these species. The homogeneous line width of the EPR signal of O_2^- is hidden in the line shape

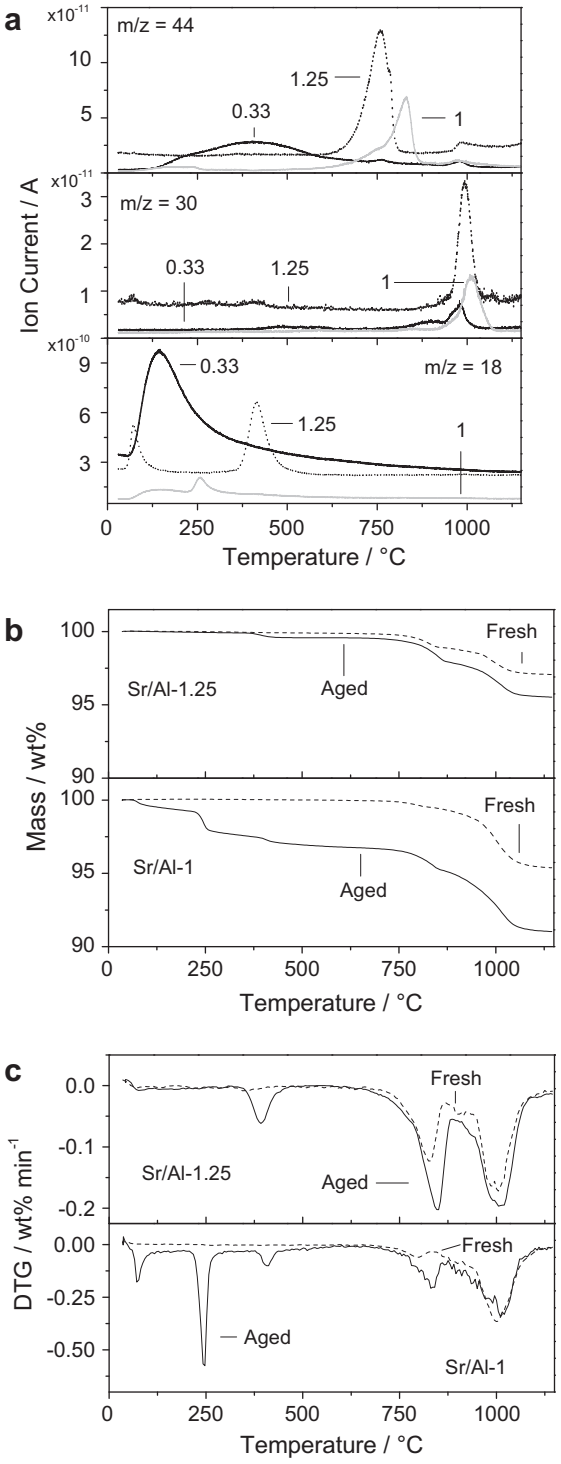

Fig. 9. TPD on Sr–Al mixed phase materials and selected single phase oxides studied by combined TG–MS. (a) MS traces of Sr/Al = 0.33, 1.0, and 1.25; (b) TG curves of fresh and aged Sr/Al-1 and Sr/Al-1.25; (c) corresponding DTG curves.

that is mainly dominated by the distribution of the *g*-tensor eigen values. Therefore, the same argumentation does not apply to these species. Still no evidence of exchange coupling between different species is observed which implies mean distances of at least 1 nm. Such relatively low density of paramagnetic centers can be determined by the concentration of active adsorption centers on the surface. On the other hand, it could also result from dimerization of nitrogen containing species which would lead to a formation of diamagnetic molecules.

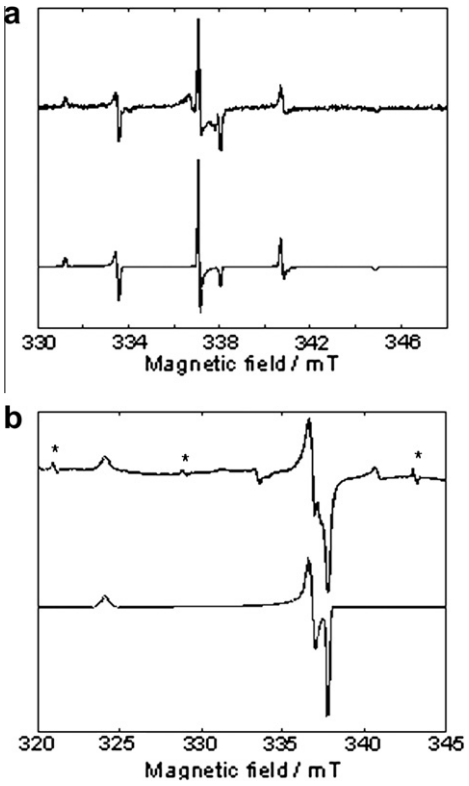

Fig. 10. Experimental and simulated EPR spectra of NO_2^{2-} and O_2^- species formed in the mixed phase oxide: (a, top) experimental EPR spectrum attributed to the surface NO_2^{2-} species measured with modulation amplitude of 0.1 mT and m.w. attenuation of 48 dB; (a, bottom) simulation of the spectrum of NO_2^{2-} with g = [2.0048, 2.0048, 1.9995] and A = [101.1, 101.1, 191.5] MHz; (b, top) experimental EPR spectrum attributed to the surface O_2 species measured with modulation amplitude of 0.3 mT and m.w. attenuation of 18 dB. The EPR signal of O_2^{2-} species is strongly saturated at these conditions. The EPR lines marked with asterisks are artefacts originating from liquid air condensed in the colder parts of the cryostat. (b, bottom) simulation of the spectrum of O_2^- with g = [2.0012, 2.0072, 2.0856] and strain of g-tensor eigen values of [0.001, 0.0018, 0.004].

Fig. 11 shows both O_2^- and NO_2^{2-} EPR signals at various experimental conditions (in a and b, respectively). Both O_2^- and NO_2^{2-} EPR signals grow in the same way upon annealing in vacuum or in O_2 atmosphere. The freshly prepared sample already contains some small amount of both species. By annealing in low vacuum (approximately 5×10^{-3} mbar), the amplitudes of the two EPR signals grow. If annealing is performed at 800 °C, the increase of the amplitude of the EPR signals is lower as compared to the annealing at 820 °C. This follows the rising part of the TPD pattern of NO (Fig. 9a). Heat treatment of the sample in O_2 atmosphere at 820 °C did not lead to a higher intensity of O_2^- or NO_2^{2-} signal as compared to the analogous treatment in vacuum.

Exposure to methane ($p \sim 100$ mbar) resulted in a significant reduction of both the O_2^- and NO_2^{2-} signals. The intensities of the two signals recovered to approximately the same level after an additional treatment in vacuum at 820 °C. Annealing in vacuum at ca. 990 °C, corresponding to complete removal of NO according to TPD, resulted in the disappearance of EPR signals of both NO_2^{2-} and O_2^-.

3.2. Catalytic results

Table 2 presents the catalytic performance of the Sr–Al single phase and mixed phase oxides along with that of the 1.9%Mn–4%Na_2WO_4/SiO_2 reference catalyst for comparison. The mixed phase oxides were more active than Al_2O_3 or $SrCO_3$ which showed only 14% and 6% conversion, respectively, at 16% and 61% selectivity to C_2 products. However, both Al_2O_3 and $SrCO_3$ were outperformed by $SrAl_4O_7$, $SrAl_2O_4$, and $Sr_3Al_2O_6$ which afforded 9%, 27%, and 22% conversion at 54%, 59%, and 51% selectivity, respectively. Further improvement in performance could be observed with the mixed phase oxides with increasing Sr/Al ratio. Plotting the conversion against the Sr/Al ratio (Fig. 12a) shows that activity consistently increased with increasing Sr loading, reaching a plateau around Sr/Al-1.25, possibly due to depletion of O_2 in the feed. The conversion and selectivity increased from 20% and 37% over Sr/Al-0.25 to a maximum of 28% and 63% over Sr/Al-1.25. Therefore, C_{2+} yield increased from 4% to 18% over these catalysts. The highest yield over Sr/Al-1.25 is comparable to that in the literature reports on Sr, Ba doped La_2O_3 [11,14]. The ethylene/ethane ratio remained about 1.5–2 over the Sr–Al oxides. Since the surface area decreased drastically with increased Sr-content (Fig. 12a), we have compared the activity per unit surface area.

The rate of methane conversion per unit surface area (mol m^{-2} h^{-1}) against the Sr/Al ratio is shown in Fig. 12b for the mixed phase oxide catalysts. It increased almost exponentially with increasing Sr-content up to a Sr/Al ratio of 1.25, reaching a maximum rate of 0.50 mol m^{-2} h^{-1}. At a Sr/Al ratio of 1.5 (Sr/Al-1.5) however, a rate of 0.11 mol m^{-2} h^{-1} was obtained. Selectivity increased to 63% at a Sr/Al ratio of 0.75 and above (Fig. 12c). $SrAl_4O_7$, $SrAl_2O_4$, and $Sr_3Al_2O_6$ showed no clear dependence of the reaction rate on the Sr-content, and rates of 0.02, 0.42 and 0.07 mol m^{-2} h^{-1} were obtained over these catalysts, respectively. The stability of the optimal catalytic system (Sr/Al-1.25) was tested in a 48 h run at 810 °C. The activity and selectivity of the catalyst proved to be stable for the duration of this long term run corroborating the good stability of the catalyst. The catalyst maintained its white color indicating that no significant carbon deposition occurred during the 48 h on stream.

To understand the effect of the Sr precursor on the catalytic performance, Sr/Al-1.25 catalysts from different Sr precursors (nitrate, hydroxide, and acetate) were additionally investigated. Catalytic data for these catalysts are included in Table 2. Evidently, the catalyst derived from Sr-acetate was the most active per unit weight, with 29% conversion, whereas the catalysts from hydroxide and nitrate precursors yielded 10% and 18% conversion, respectively. The corresponding reaction rates referred to unit surface area were 0.54, 0.30, and 0.14 mol m^{-2} h^{-1} over the hydroxide, nitrate, and acetate derived catalysts, respectively.

The activity of the Sr–Al-based catalysts was compared to that of 1.9%Mn–4%Na_2WO_4/SiO_2, a well-known catalyst for this reaction [33,35,74]. The reference catalyst showed 18% methane conversion at 68% selectivity, and a reaction rate of 0.32 mol m^{-2} h^{-1}, significantly lower than the optimal Sr–Al material (0.50 mol m^{-2} h^{-1} for Sr/Al-1.25). Furthermore, the C_{2+} yield was also significantly lower. Note that the catalytic performance of the reference catalyst was higher than the values reported in literature [35] (0.32 vs. 0.07 mol m^{-2} h^{-1}), which might be due to the different experimental conditions, such as the CH_4/O_2 ratio (7.5 in [35] vs. 5 in this work) and temperature (785 °C in [35] vs. 810 °C). Finally, it may also be worthwhile to compare the performance of Sr/Al-1.25 with that of another well-known reference catalyst for OCM, 5%Sr/La_2O_3. In an earlier study [20], we observed a methane conversion rate of 0.3 mol m^{-2} h^{-1} and a slightly lower C_{2+} yield of 16% for this catalyst under almost similar conditions (total O_2 conversion at 730 °C). Thus, we can conclude that Sr/Al-1.25 shows a catalytic performance in OCM which is at least comparable to these well-known and active OCM catalysts.

3.3. Discussion

The main objective of this study was to investigate the potential of Sr–Al–O based catalysts for oxidative coupling of methane. The

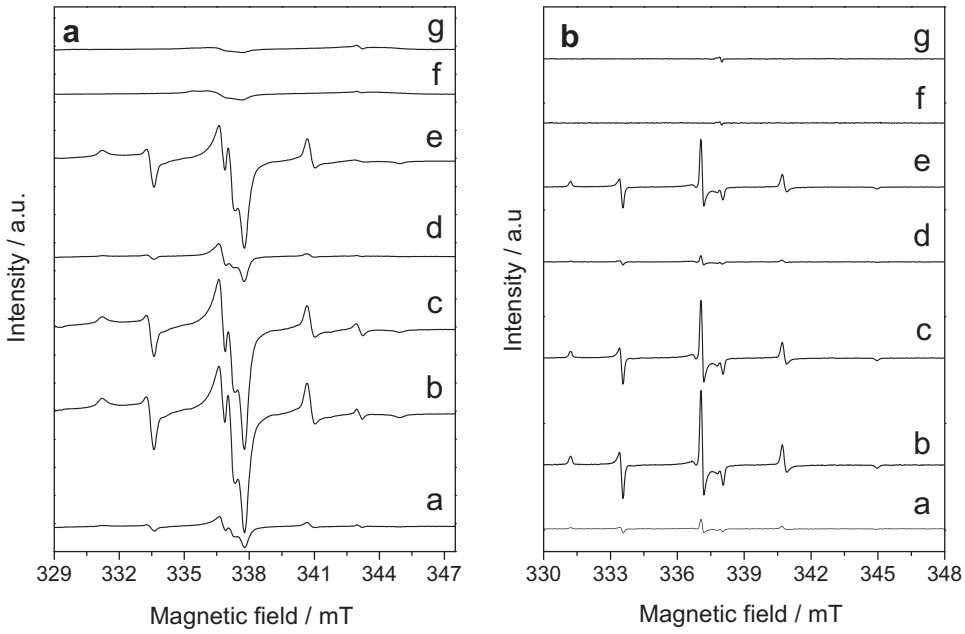

Fig. 11. Change of the EPR signals of O_2^- (**a**, left) and NO_2^{2-} (**b**, right) species upon sample treatment for the mixed phase oxide sample: (a) freshly prepared sample; (b) sample after annealing in low vacuum at 820 °C for 20 min; (c) after an additional treatment in O_2 atmosphere (1 bar) for 20 min at 820 °C; (d) after a treatment in methane atmosphere (0.1 bar) for approx. 30 min at 820 °C; (e) after an additional annealing in low vacuum for 20 min at 820 °C; (f) after an annealing in low vacuum at approx. 990 °C; (g) after an annealing in O_2 atmosphere at 820 °C. All the treatments (a)–(g) were performed stepwise with the same sample. Registration conditions for O_2^-: modulation amplitude 0.3 mT, microwave attenuation 18 dB; for O_2^{2-}: modulation amplitude 0.1 mT, microwave attenuation 48 dB. EPR spectra were registered at 130 K.

structural dependence of the catalytic behavior was investigated by varying the elemental composition of Sr–Al oxides as well as their phase composition, ranging from single phase oxides and mixed phase oxides derived via different synthesis procedures. The catalytic studies indicate that for the oxidative coupling of methane, the mixed phase oxides are more active and selective than the single phase oxides. The rate of methane conversion per unit surface area over the mixed phase oxides increased almost exponentially with increasing Sr/Al ratio, from 0.001 for Al_2O_3 to 0.50 mol m^{-2} h^{-1} for Sr/Al-1.25 (Fig. 12b). The activity improved with increasing Al^{IV}/Al^{VI} ratio, which reflects the increase of the fraction of tetrahedrally coordinated Al in the materials. The increase in the rate of methane conversion referred to the unit surface is attributed to an increase in the density and/or activity of the sites responsible for oxide radical formation. However, a possible influence of the greatly different surface area of the various catalysts (Fig. 12a) on the radical coupling and trapping, as well as chain termination cannot be ruled out. Note that selectivity showed a different dependence on the Sr/Al ratio (Fig. 12c).

The specific surface area of the Sr/Al oxides decreased strongly with increasing Sr-content (Fig. 12a). Clearly, the synthesis procedure results in rather large particles. Based on the TG–MS and EPR results, the as-prepared catalysts contain a certain fraction of residual nitrates. Unreacted precursor salts (either Al- or Sr-based) are the only likely source of these nitrates, and based on their rather high temperature of decomposition, these are probably trapped inside larger particles. High temperature treatment (>860 °C) causes these nitrates to decompose and diffuse to the surface where their remnants adsorb as NO_2^{2-} and O_2^- species, as evidenced by EPR. Their potential contribution to the OCM reaction is discussed below.

From XRD, the $Sr_3Al_2O_6$ double perovskite phase was found to be the dominating crystalline phase in the catalysts, its relative intensity increasing at higher Sr/Al ratios (Figs. 1 and 2). Also, by NMR evidence of this phase was found, in the form of Al^{IV} species [48,75] at 65 ppm in the 1D (Fig. 5) and by two ridges in the 2D experiments (Fig. 7). These well-ordered Al^{IV} species were revealed to be present in the as-prepared Sr/Al-1.25, and undoubtedly belong to the double perovskite crystal phase. Diffraction also provided evidence of a hydrated Sr–Al compound ($Sr_3Al_4O_9{\cdot}2H_2O$). Corroborating data was obtained by ^{27}Al NMR, where a substantial signal due to octahedrally coordinated Al species was observed. This narrow signal had an increasing intensity with increasing Sr/Al ratio and could indicate the presence of a $Sr_3Al_2(OH)_{12}$ hydrogarnet phase [76]. The reaction of $Sr_3Al_2O_6$ with water is known to proceed at mild conditions [75], and has probably occurred by reaction of ambient water with the perovskite phase in the as-prepared material. The presence of bulk-like hydrated species or hydroxides was implied as well by TG–MS analysis (Fig. 9b and c) of catalysts stored under ambient conditions. The temperature of decomposition shows these compounds not to be stable at reaction conditions (i.e., 810 °C). This was supported by 2D NMR, where calcination of Sr/Al-1.25 at 1000 °C resulted in disappearance of the Al^{VI} species and led to more ordered Al^{IV} species (Fig. 7a and b).

Although the hydroxides or hydrogarnet phases are thermally unstable under reaction conditions, a significant difference in activity was observed between fresh (i.e., used within 3 h after synthesis) and stored catalysts (9 instead of 28% conversion). By TG–MS, two differences between fresh and stored catalysts were observed: stored catalysts showed sharp weight loss features due to decomposition of hydroxides or hydrated species below 800 °C, whereas above this temperature stored catalysts showed a higher weight loss due to decomposition of carbonate species. These differences are highlighted by the DTG traces in Fig. 9c.

Although the origin of the loss of activity is unclear, it seems to indicate that the species formed during storage do not completely revert to their starting compound upon decomposition. Differences in the thermal stability of these new species might result in local deviations of the bulk Sr/Al ratio, a parameter known to be crucial in the genesis Sr/Al oxides [47,48]. Depending on the (local) concentration of the elements, very different (meta)stable phases can be obtained [47,48]. At any rate, care must be taken to avoid exposure of the catalysts to ambient water or carbon dioxide when applying these catalytic materials.

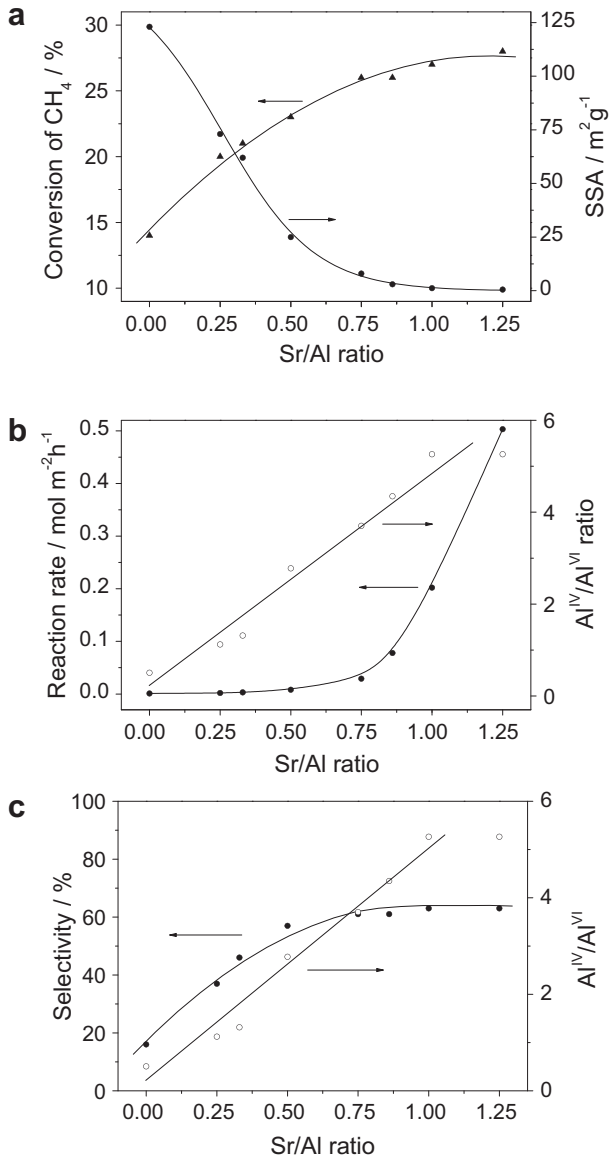

Fig. 12. (a) Dependence of methane conversion and specific surface area (SSA) on the composition (Sr/Al ratio) of Sr–Al mixed phase oxides. (b) Rate of methane conversion per unit surface area and Al^{IV}/Al^{VI} ratio at varying Sr/Al ratio in the mixed phase oxides. (c) Dependence of selectivity and Al^{IV}/Al^{VI} ratio on composition of the mixed phase oxides. The lines are drawn to guide the eye.

The above shows that in the Sr/Al series of oxides, two crystalline phases coexist, and based on the broad line shapes in the 2D MQMAS spectra, a significant portion of the Al is in a less ordered environment, and as a consequence poorly characterizable by XRD and NMR. Additionally, TG–MS showed the presence of nitrate and carbonate containing compounds. Since such a situation does not facilitate the identification of the compounds active in OCM, a number of model systems were synthesized for means of comparison. Three single phase oxides, $SrAl_4O_7$, $SrAl_2O_4$, and $Sr_3Al_2O_6$ were tested and characterized in order to provide clues on the activity of Sr-poor to Sr-rich single crystalline phases. Note that the as-prepared $Sr_3Al_2O_6$ double perovskite contained a fraction of $Sr_3Al_2(OH)_{12}$ hydrogarnet, which at the temperature at which OCM was conducted would have decomposed into the corresponding double perovskite phase [76]. Therefore, we consider the activity of this material to be representative for $Sr_3Al_2O_6$ double perovskite phase.

The reaction rates observed for these oxides (Table 2), did not show a trend with increasing Sr-content as opposed to the Sr/Al materials. Comparing the reaction rates of these single phase oxides with the Sr/Al series, it becomes evident that for the double perovskite very similar reaction rates are observed compared to the Sr/Al-material of the same composition, indicating a similarity in the active phases present. Apparently, the double perovskite is not extremely active in OCM. When $SrAl_4O_7$ and $SrAl_2O_4$ are compared with the Sr/Al materials of the same composition, it shows that these single phase oxides are more active per unit surface area, and the more Sr-rich material displays a higher reaction rate. As follows from XRD and NMR analysis, the Sr/Al-0.25 and 0.5 mixed phase oxides contained $Sr_3Al_4O_9{\cdot}2H_2O$ along with a significant fraction of Al_2O_3 (and $Sr_3Al_2O_6$ for Sr/Al-0.5), which apparently possess a lower density in active sites as the single phase oxides.

Since from the Sr/Al series, the highest activity was obtained for the composition with a Sr/Al ratio of 1.25, three catalysts with the same composition were prepared via a different synthesis route and from different Sr precursors (see Section 2). The lowest reaction rate was obtained for Sr/Al-1.25A, which contained a large fraction of $SrCO_3$ with some $Sr_3Al_2O_6$. Apparently, the presence of the carbonate is detrimental for the catalytic activity, a conclusion which could also be drawn from the comparison between the fresh and stored catalysts. The highest activity, expressed as rate per unit surface area, was observed for the impregnated Al_2O_3 supported catalyst Sr/Al-1.25H, which had an activity roughly comparable to that of Sr/Al-1.25. Interestingly, the Sr/Al-1.25H catalyst consisted of a mixture of $Sr_3Al_2O_6$ and $Sr_{12}Al_{14}O_{33}$ crystalline phases, the latter has been shown to be able to form oxygen radicals [47]. By 2D NMR, an additional well-ordered Al^{IV} site was observed for this material (Fig. 7c), slightly above the ridges belonging to $Sr_3Al_2O_6$. Since no other crystalline phases were observed, we tentatively attribute this feature to the $Sr_{12}Al_{14}O_{33}$ crystalline phase.

The 2D NMR experiments revealed that the Sr/Al-1.25 and Sr/Al-1.25H materials shared a number of similarities. The two clear ridges, tentatively ascribed to the double perovskite phase, are found in both materials, corroborating the analysis of the diffractograms. Additional features, indicating a well-ordered Al^{IV} species were found in Sr/Al-1.25H, located between the double ridges and the symmetrical feature at 70 ppm. The area of the latter feature falls in the area of the less ordered species in Sr/Al-1.25. Although position and shape are different, it shows that both materials possess a certain fraction of Al species with rather similar (tetrahedral) environments. The similarities in these Al^{IV} environments could suggest that formation of radicals can occur, as reported for $Sr_{12}Al_{14}O_{33}$ [47]. On the other hand, Sr could also be substituted in the non-crystalline alumina phase producing oxide ion vacancies and due to the increase in surface basicity, the formation of oxygen radical species may be enhanced. The increase in basicity of the surface was indicated by XPS showing formation of carbonate with increasing Sr/Al ratio.

It has been proposed that O_2^- radicals initiate the OCM reaction [36]. Therefore, the presence of O_2^- radicals on the catalyst surface is of particular significance, since they could constitute the active species. Although the O_2^- radicals observed by EPR are likely a decomposition product of trapped nitrates, the results obtained by EPR indicate that the surface is able to stabilize O_2^- radicals. The loss in signal intensity after exposure to methane demonstrates that these radicals are able to react, and can therefore indeed play a role in the OCM reaction. For in-depth mechanistic insight, however, more research would be needed.

As the observed radicals were being formed from a finite nitrate reservoir in these catalytic systems, the question arises whether the activity of these materials is indeed catalytic in nature, or

whether the decomposition products are directly responsible for the activity instead. There are a couple of strong arguments against the latter scenario. Firstly, the catalytic activity remained constant during long term experiments of 48 h. In this time period, about 4 mol of methane was converted, which is several orders of magnitude larger than the amount of nitrate in the catalyst (0.0005 mol, if we very conservatively assume all Sr to be in the form of $Sr(NO_3)_2$). Secondly, Sr/Al-1.25 materials prepared from other precursor materials such as hydroxide and acetate (see Table 2 for catalytic results, and Section 2 for description of synthesis) exhibited comparable activity and selectivity, clearly demonstrating that the nitrate impurities are not contribution significantly to the activity observed.

4. Conclusions

Sr–Al mixed oxides proved to be a promising class of catalysts for the oxidative coupling of methane. The Sr–Al mixed oxides prepared by co-precipitation were mainly made up of two phases: $Sr_3Al_2O_6$ as a major and $Sr_3Al_4O_9{\cdot}2H_2O$ as a minor crystalline phase. However, beside these two crystalline phases, solid state NMR and TG–MS studies revealed the presence of several other, non-crystalline species. Materials prepared via other preparation route and precursors yielded $Sr_3Al_2O_6$ as major crystalline phase as well, along with Sr-carbonate from acetate and $Sr_{12}Al_{14}O_{33}$ from Sr-hydroxide precursors.

Although above a relatively low Sr/Al ratio (0.5), almost only $Sr_3Al_2O_6$ was observed by XRD, solid state NMR showed that the Al^{IV}/Al^{VI} ratio increased with increasing Sr-content up to Sr/Al-1.25. It further revealed the presence of a less ordered phase in the Sr–Al mixed oxides. This phase could be a Sr substituted γ-Al_2O_3 in non-crystalline phase and therefore, presence of oxygen ion vacancies could be possible due to charge balance producing four coordinated Al species. Increase in the Al^{IV}/Al^{VI} ratio was paralleled by an increase in conversion and less prominently in selectivity of these Sr–Al oxide materials, albeit the specific surface area decreased strongly. Methane conversion rate per unit surface area increased steeply at higher Sr/Al ratio in the mixed phase oxides. Most probably oxygen ion vacancies in the non-crystalline phase promote oxygen radical formation at higher basicity.

Above a Sr/Al ratio of 1.25, poorly active mixed oxides were obtained, probably due to formation of a thicker layer of hydroxide or carbonate species on the surface. The facile formation of a carbonate and hydroxide layer also likely contributed to the lower activity of materials stored under ambient conditions. Under the test conditions used, the optimal Sr/Al catalyst outperformed a 1.9%Mn–4%Na_2WO_4/SiO_2 reference catalyst in terms of activity and C_{2+} yield, which hints toward a significant catalytic potential of this class of materials for the oxidative coupling of methane. However, a final assessment of this potential requires further testing where a broader variation of the experimental conditions (temperature, space velocity, methane/oxygen ratio, etc.) is applied.

Acknowledgments

We kindly acknowledge financial support by ETH Zurich (TH-09 06-2). We thank Dr. Frank Krumeich for the electron microscopy study, which was performed at EMEZ (Electron Microscopy ETH Zurich).

References

[1] G.E. Keller, M.M. Bhasin, J. Catal. 73 (1982) 9.
[2] J.S. Lee, S.T. Oyama, Catal. Rev.-Sci Eng. 30 (1988) 249.
[3] G.J. Hutchings, M.S. Scurrell, J.R. Woodhouse, Chem. Soc. Rev. 18 (1989) 251.
[4] J. Carreiro, M. Baerns, J. Catal. 117 (1989) 258.
[5] J.H. Lunsford, Angew. Chem.-Int. Ed. 34 (1995) 970.
[6] T. Ito, J.H. Lunsford, Nature 314 (1985) 721.
[7] Y. Tong, J.H. Lunsford, J. Chem. Soc., Chem. Commun. 11 (1990) 792.
[8] S. Hou, Y. Cao, W. Xiong, H. Liu, Y. Kou, Ind. Eng. Chem. Res. 45 (2006) 7077.
[9] A. Malekzadeh, A.K. Dalai, A. Khodadadi, Y. Mortazavi, Catal. Commun. 9 (2008) 960.
[10] F. Papa, L. Patron, O. Carp, C. Paraschiv, B. Ioan, J. Mol. Catal. A: Chem. 299 (2009) 93.
[11] J.M. Deboy, R.F. Hicks, J. Chem. Soc., Chem. Commun. (1988) 982.
[12] J.M. Deboy, R.F. Hicks, Ind. Eng. Chem. Res. 27 (1988) 1577.
[13] J.-L. Dubois, C.J. Cameron, Appl. Catal. 67 (1990) 49.
[14] H. Yamashita, Y. Machida, A. Tomita, Appl. Catal. A: Gen. 79 (1991) 203.
[15] V.R. Chaudhary, V.H. Rane, J. Catal. 130 (1991) 411.
[16] V.R. Chaudhary, B.S. Uphade, S.A.R. Mulla, Ind. Eng. Chem. Res. 36 (1997) 3594.
[17] V.R. Chaudhary, S.A.R. Mulla, V.H. Rane, J. Chem. Technol. Biotechnol. 72 (1998) 125.
[18] K. Otsuka, K. Jinno, A. Morikawa, J. Catal. 100 (1986) 353.
[19] J.-L. Dubois, B. Rebours, C.J. Cameron, Appl. Catal. 67 (1990) 73.
[20] T. Baidya, N.V. Vegten, Y. Jiang, F. Krumeich, A. Baiker, Appl. Catal. A: Gen. 391 (2011) 205.
[21] K. Aika, T. Moriyama, N. Takasaki, E. Iwamatsu, J. Chem. Soc., Chem. Commun. (1986) 1210.
[22] T. Ito, J.X. Wang, C.H. Lin, J.H. Lunsford, J. Am. Chem. Soc. 107 (1985) 5062.
[23] G. J Hutchings, M.S. Scurrell, J.R. Woodhouse, J. Chem. Soc. Chem. Commun. (1987) 1862.
[24] E. Iwamatsu, T. Moriyama, N. Takasaki, K. Aika, J. Chem. Soc., Chem. Commun. (1987) 19.
[25] J.A.S.P. Carreiro, M. Baerns, J. Catal. 117 (1989) 258.
[26] T. Nishiyama, T. Watanabe, K. Aika, Catal. Today 6 (1990) 391.
[27] K. Aika, N. Fujimoto, M. Kobayashi, E. Iwamatsu, J. Catal. 127 (1991) 1.
[28] Process for the oxidative coupling of methane to higher hydrocarbons, US5132482, 1992
[29] A.M. Maitra, Appl. Catal. A: Gen. 104 (1993) 11.
[30] A.M. Maitra, Appl. Catal. A: Gen. 114 (1994) 65.
[31] R. Voyatzis, J.B. Moffat, J. Catal. 142 (1993) 45.
[32] X.P. Fang, S.B. Li, J.Z. Lin, J.F. Gu, D.X. Yang, J. Mol. Catal. (China) 6 (1992) 427.
[33] D.J. Wang, M.P. Rosynek, J.H. Lunsford, J. Catal. 155 (1995) 390.
[34] A. Palermo, J.P.H. Vazquez, A.F. Lee, M.S. Tikhov, R.M. Lambert, J. Catal. 177 (1998) 259.
[35] S. Pak, P. Qiu, J.H. Lunsford, J. Catal. 179 (1998) 222.
[36] C.H. Lin, K.D. Campbell, J.X. Wang, J.H. Lunsford, J. Phys. Chem. 90 (1986) 534.
[37] C. Louis, T.L. Chang, M. Kermarec, T.L. Van, J.M. Tatibouet, M. Che, Colloids Surf. A 72 (1993) 217.
[38] F. Freund, G.C. Maiti, F. Battlo, M. Baerns, J. Chim. Phys. & Phys.-Chim. Biol. 87 (1990) 1467.
[39] M.S. Palmer, M. Neurock, M.M. Olken, J. Am. Chem. Soc. 124 (2002) 8452.
[40] S.J. Korf, J.A. Roos, J.M. Diphoorn, R.H.J. Veehof, J.G. van Ommen, J.R.H. Ross, Catal. Today 4 (1989) 279.
[41] A.G. Anshits, E.N. Voskresenskaya, L.I. Kurteeva, Catal. Lett. 6 (1990) 67.
[42] D.J. Ilett, M.S. Islam, J. Chem. Soc. Faraday Trans. 89 (1993) 3833.
[43] M.S. Islam, D.J. Ilett, Solid State Ionics 72 (1994) 54.
[44] H. Borchert, M. Baerns, J. Catal. 168 (1997) 315.
[45] Z. Taheri, N. Sayed-Martin, A.A. Safekordi, K. Nazari, S.Z. Pashne, Appl. Catal. A: Gen. 354 (2009) 143.
[46] A.M. Maitra, I. Campbell, R.J. Tytler, Appl. Catal. A: Gen. 85 (1992) 27.
[47] K. Hayashi, N. Udea, S. Matsuishi, M. Hirano, T. Kamiya, H. Hosono, Chem. Mater. 20 (2008) 5987.
[48] O. Yamaguchi, A. Narai, K. Shimizu, J. Am. Ceram. Soc. 69 (1986) C36.
[49] A. Douy, M. Capron, J. Eur. Ceram. Soc. 23 (2003) 2075.
[50] K. Vishista, F.D. Gnanam, J. Eur. Ceram. Soc. 29 (2009) 77.
[51] P. Escribano, M. Marchal, M.L. Sanjuan, P. Alonso-Gutierrez, B. Julian, E. Cordoncillo, J. Solid State Chem. 178 (2005) 1978.
[52] Y. Xu, Y. He, X. Yuan, Powder Technol. 172 (2007) 99.
[53] Y.B. Xu, P.X. Lu, G.H. Huang, C.L. Zeng, Mater. Chem. Phys. 95 (2006) 62.
[54] K.C. Patil, S.T. Aruna, T. Mimani, Curr. Opin. Solid State Mater. Sci. 6 (2002) 507.
[55] Z.C. Jiang, C.J. Yu, X.P. Fang, S.B. Li, H.L. Wang, J. Phys. Chem. 97 (1993) 12870.
[56] S.P. Brown, S. Wimperis, J. Magn. Reson. 124 (1997) 279.
[57] S.P. Brown, S. Wimperis, J. Magn. Reson. 128 (1997) 42.
[58] J.-P. Amoureux, C. Fernandez, Triple, quintuple and higher order multiple quantum MAS NMR of quadrupolar nuclei, Solid State NMR 10 (1998) 211–223.
[59] J.-P. Amoureux, C. Fernandez, Erratum to "Triple, quintuple and higher order multiple quantum MAS NMR of quadrupolar nuclei" [Solid State NMR 10 (1998) 211–223], Solid State NMR 16 (2000) 339–343.
[60] J.D. van Beek, J. Magn. Reson. 187 (2007) 19.
[61] S. Stoll, A. Schweiger, J. Magn. Reson. 178 (2006) 42. <www.easyspin.org>.
[62] J. Huang, Y. Jiang, V.R.R. Marthala, B. Thomas, E. Romanova, M. Hunger, J. Phys. Chem. C 112 (2008) 3811.
[63] H. Ernst, D. Freude, H. Pfeifer, I. Wolf, in: J. Weitkamp, H.G. Karge, H. Pfeiffer, W. Holderlich (Eds.), Zeolites and Related Microporous Materials: State of the Art, vol. 84, Elsevier, Amsterdam, 1994, p. 381.
[64] D. Dissanayake, J.H. Lunsford, M.P. Rosynek, J. Catal. 143 (1993) 286.
[65] K. Hayashi, M. Hirano, S. Matsuishi, H. Hosono, J. Am. Chem. Soc. Commun. 124 (2002) 738.
[66] M. Chiesa, E. Giamello, M. Che, Chem. Rev. 110 (2010) 1320.
[67] J.H. Lunsford, J. Chem. Phys. 46 (1967) 4347.

[68] P.H. Kasai, R.J. Bishop Jr., J. Am. Chem. Soc. 94 (1972) 5560.
[69] C. Decarne, E. Abi-Aad, A. Aboukaïs, Catal. Lett. 62 (1999) 45.
[70] S. Livraghi, M.C. Paganini, M. Chiesa, E. Giamello, Res. Chem. Intermed. 33 (2007) 739.
[71] C. Di Valentin, G. Pacchioni, M. Chiesa, E. Giamello, S. Abbet, U. Heiz, J. Phys. Chem. B 106 (2002) 1637.
[72] M. Anpo, N. Aikawa, Y. Kubokawa, M. Che, C. Louis, E. Giamello, J. Phys. Chem. 89 (1985) 5689.
[73] G. Jeschke, Y. Polyhach, Phys. Chem. Chem. Phys. 9 (2007) 1895.
[74] S. Pak, J.H. Lunsford, Appl. Catal. A: Gen. 168 (1998) 131.
[75] B.C. Chakoumakos, G.A. Lager, J.A. Fernandez-Baca, Acta Cryst. C48 (1992) 414.
[76] G. Li, S. Feng, L. Li, X. Li, W. Jin, Chem. Mater. 9 (1997) 2894.